

Supporting Information

**Anion Endowed High Dielectric Water-Deficient Interface towards**

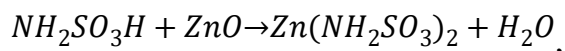
**Ultrastable Zn Metal Battery**

Xiangjie Liu<sup>a</sup>, Xiaoxin Nie<sup>a</sup>, Yujiao Yang<sup>a</sup>, Meng Yao<sup>b,\*</sup>, Hanfeng Liang<sup>c,\*</sup>, Mi Zhou<sup>d</sup>,  
Jin Zhao<sup>e</sup>, Du Yuan<sup>a,\*</sup>

## Experimental details

### *Synthesis of Electrolytes*

Zinc sulfamate ( $Zn(SA)_2$ ) was prepared by dissolving ZnO in aqueous solution of  $NH_2SO_3H$  with stoichiometric molar ratio,



followed by drying at 80 °C for 12 hours to obtain the powder form.  $Zn(SA)_2$  solutions of different concentrations (i.e. x mol of  $Zn(SA)_2$ , x=2,4) were then prepared by dissolving the obtained powder in deionized (DI) water. And the PH values of 4M and 2M  $Zn(SA)_2$  were measured to be 3.48 and 3.72 respectively.

Commercial zinc trifluoromethanesulfonate ( $Zn(OTf)_2$ ) salts (98%, Ningbo Merak Advanced Materials Technology Co., Ltd) were used to prepare the corresponding aqueous electrolytes.

### *Material Characterizations*

X-ray diffraction (XRD) spectra were collected on a Bruker D8 Advance A25 X with Cu  $K\alpha$  irradiation ( $\lambda=1.5418 \text{ \AA}$ ). The Fourier transform infrared spectroscopy (FTIR-ATR) was recorded by Shimadzu Instrument IRTracer-10 with the attenuated total reflectance compartment. Scanning electron microscopy (SEM) images and energy dispersive X-ray spectra (EDX) of the electrode were collected on a JSM-7900F. XPS spectra were collected by Kratos AXIS Supra XPS with dual anode (Al/Ag  $K\alpha$ ) X-ray monochromatic source.

### *Molecular dynamic (MD) simulations*

All solution components were randomly packed into cubic simulation boxes. All MD simulations were carried out by Forcite module with COMPASS III force field<sup>1,2</sup> in Materials Studio (MS) 2020. Van der Waals and Coulomb interactions were respectively considered by atom based and Ewald methods with a cut-off value of 12.5  $\text{\AA}$ . Equations of motion were integrated with a time step of 1 fs. After energy minimization, the electrolyte system was fully relaxed under periodic boundary conditions for 400 ps in the NPT ( $P = 1$  atmosphere,  $T = 293.0$  K) ensemble using the Nose thermostat and Berendsen barostat, which was long enough for system temperature, potential and total energy to get stable. After reaching equilibrium state, another 400 ps simulation under NVT ensemble was performed to extract trajectory and data for radial distribution function (RDF) and coordination number (CN) calculation. The dynamic trajectory for each system was outputted at an interval of 4 ps. The coordination number  $N_i$  of atom  $i$  in the first solvation shell surrounding  $Zn^{2+}$  was calculated as:

$$N_i = 4\pi\rho^0 \int_0^{R_M} g(r)r^2 dr$$

in which  $R_M$  is the distance of the first minimum following the first peak in the RDF  $g(r)$  and  $\rho$  is the number density of atom  $i$ .

### DFT calculations

The binding energies between  $\text{Zn}^{2+}$  and  $\text{H}_2\text{O}$ ,  $\text{SA}^-$  and corresponding electrostatic potentials (ESP) were respectively calculated by Dmol3 module in MS 2020 in MS. Firstly, the generalized gradient approximation (GGA) with Perdew–Burke–Ernzerhof (PBE) exchange-correlation functional was employed to fully relax  $\text{H}_2\text{O}$ ,  $\text{SA}^-$  and The double-numeric quality basis sets with polarization functions were used. The iterative tolerances for energy change, force and displacements were  $1 \times 10^{-5}$  Ha, 0.002 Ha  $\text{\AA}^{-1}$  and 0.005  $\text{\AA}$ , respectively. In the self-consistent field (SCF) procedure,  $10^{-6}$  a.u. was used for the convergence standard electron density. After structure optimization, the Adsorption Locator Tools<sup>4</sup> in MS were used to locate  $\text{Zn}^{2+}$  at energy favorable site of  $\text{H}_2\text{O}$ ,  $\text{SA}^-$  and. Then each interaction pair was freely optimized by Dmol3 module. Finally, single point energy calculation was executed and meanwhile the ESP was outputted. The binding energies  $E_b$ <sup>5,6</sup> were calculated according to the following equation:

$$E_b = E_{total} - E_{adsorbent} - E_{\text{Zn}^{2+}}$$

Where  $E_{total}$  is the total energy of the optimized adsorption structure,  $E_{adsorbent}$  is the energy of  $\text{H}_2\text{O}$ ,  $\text{SA}^-$ ,  $E_{\text{Zn}^{2+}}$  is the energy of one  $\text{Zn}^{2+}$ .

### Electric Polarizability

The electric polarizability  $\alpha$  in isotropic media is defined as the ratio of the induced dipole moment  $p$  of an atom to the electric field  $E$  that produces this dipole moment.

$$\alpha = \frac{|p|}{|E|}$$

Polarizability has the SI units of  $\text{C} \cdot \text{m}^2 \text{V}^{-1} = \text{A}^2 \cdot \text{s}^4 \cdot \text{kg}^{-1}$  while its cgs unit is  $\text{cm}^3$ . Usually it is expressed in cgs units as a so-called polarizability volume, sometimes expressed in  $\text{\AA}^3 = 10^{-24} \text{ cm}^3$ . One can convert from SI units ( $\alpha$ ) to cgs ( $\alpha'$ ) as follows:

$$\alpha' (\text{cm}^3) = \frac{10^6}{4\pi\epsilon_0\alpha (\text{C} \cdot \text{m}^2 \text{V}^{-1})} = \frac{10^6}{4\pi\epsilon_0\alpha (\text{F} \cdot \text{m}^2)} \cong 8.988 \times \alpha (\text{F} \cdot \text{m}^2)$$

where  $\epsilon_0$ , the vacuum permittivity, is  $\sim 8.854 \times 10^{-12}$  ( $\text{F m}^{-1}$ ). If the polarizability volume

in cgs units is denoted  $\alpha'$  the relation can be expressed generally (in SI) as  $\alpha = 4\pi\epsilon_0\alpha'$ .

And the polarizability of individual particles is related to the average electric susceptibility of the medium by the Clausius-Mossotti relation:

$$R = \left(\frac{4\pi}{3}\right)N_A\alpha_c = \left(\frac{M}{p}\right)\left(\frac{\epsilon_r - 1}{\epsilon_r + 2}\right)$$

Where  $R$  is the molar refractivity,  $N_A$  is the Avogadro constant,  $\alpha_c$  is the electronic polarizability,  $p$  is the density of molecules,  $M$  is the molar mass, and  $\epsilon_r = \epsilon/\epsilon_0$  is the material's relative permittivity or dielectric constant (or in optics, the square of the refractive index).

### Electrochemical characterizations

The dielectric properties ( $\epsilon_r$ ) of different electrolytes were measured by Electrochemical Impedance Spectroscopy (EIS) for the assembled SS|electrolyte/membrane|SS configuration, and calculated by

$$\epsilon_r = -\frac{Z'' d}{2\pi f |Z| \epsilon_0 A},$$

where  $\epsilon_0$  is the vacuum permittivity,  $d$  and  $A$  are the thickness and area of the glass fiber. And EIS analysis provides complex and imaginary impedance ( $Z$  and  $Z''$ ), frequency  $f$ .

Cyclic voltammetry (CV) was carried out to determine the EWs of electrolytes by DH 7000 (Jiangsu Donghua Analytical Instrument Co., Ltd.) in a two-electrode cell with Pt foil as the work electrode, Zn foil (100, 200  $\mu\text{m}$ ) as the counter electrode, at a scan rate of 1  $\text{mV s}^{-1}$ . Tafel curves were conducted in a three-electrode configuration, with commercial Zn foil as the working electrode, leakless type Ag/AgCl as the reference electrode, Pt as the counter electrode, and Zn(SA)<sub>2</sub> electrolytes. EIS spectra are characterized using the DH 7000 electrochemical workstation, with a frequency range from 0.1 Hz to 1.0 MHz and a current amplitude of 10 mV. Ionic conductivities of electrolytes were measured by FE38 conductivity meter (Mettler Toledo). The capacitance–potential curves were measured in the alternating current voltammetry tests. The frequency is 6 Hz and the amplitude ( $A$ ) is 5 mV. The selective region of phase angles was 0° and 90°. The calculation of capacitance is based on the method proposed by Arrigan et al<sup>7,8</sup>. To calculate the transference number, current-time curve of Zn|Zn symmetric cell with electrolytes were measured after a constant potential of 10 mV. EIS spectra were collected before and after measurement. From chronoamperometry and impedance data, the Zn<sup>2+</sup> transference number ( $t_{\text{Zn}^{2+}}$ ) was calculated by the following equation<sup>9,10</sup>:

$$t_{\text{Zn}^{2+}} = \frac{I_S(\Delta V - I_0 R_0)}{I_0(\Delta V - I_S R_S)},$$

where  $\Delta V$  is the applied constant polarization (10 mV),  $I_0$  and  $R_0$  are the initial current and resistance, and  $I_S$  and  $R_S$  are the steady-state current and resistance, respectively.

Note that the resistances here refer to the charge transfer resistances. The CP curve is conducted in the Cu|Zn half-cell with a current density of 1  $\text{mA cm}^{-2}$ , and the CA curve is also conducted in the Cu|Zn half-cell with an overpotential of 150 mV.

For CA curve, Scharifker–Hills model was applied, which allows determining the type

of nucleation by analyzing the ascending parts of the chronoamperometry prior to the overlap of nuclei diffusion zones<sup>11</sup>.

#### *V<sub>2</sub>O<sub>5</sub>/Zn full cell*

V<sub>2</sub>O<sub>5</sub> nanosheets were synthesized in large scale and the electrode preparation was conducted based on the previous report<sup>12</sup>. Briefly, the slurry was formulated by the synthesized V<sub>2</sub>O<sub>5</sub> and Super P (TIMCAL) in a weight ratio of 8:2. After casting and vacuum drying, the binder-free electrode on stainless steel mesh was with a mass loading of active material ~1.5-2 mg cm<sup>-2</sup>. The coin cells were assembled using the casted electrodes, commercial Zn foils, and aqueous electrolytes of Zn(SA)<sub>2</sub> and Zn(OTf)<sub>2</sub>. ~60 μL of electrolyte was applied following common practice. The galvanostatic charge/discharge curves were measured in the potential range of 0.3-1.8V by Neware battery tester.

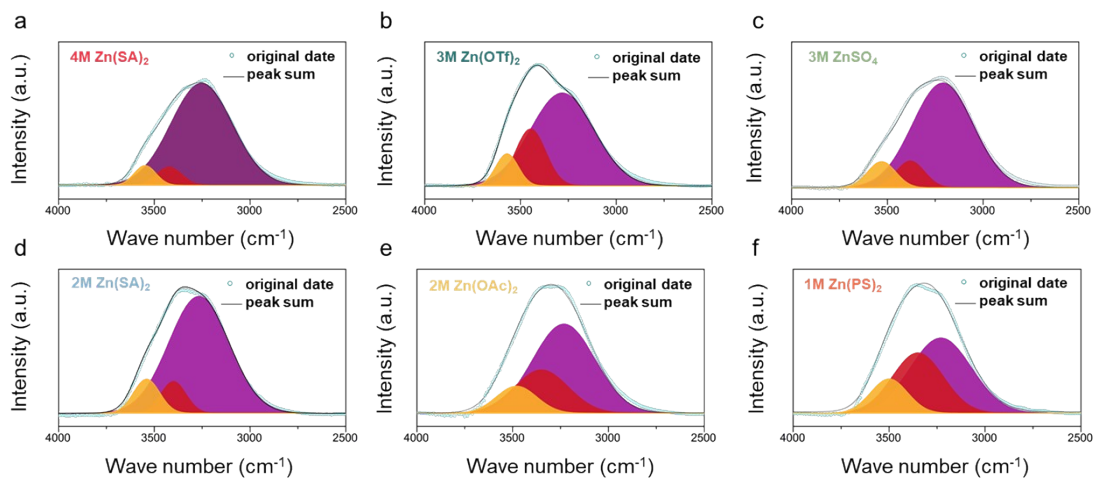


**Figure S1.** Deconvolution on the  $-OH$  vibrational features of saturated aqueous zinc electrolytes: (a) 4M  $Zn(SA)_2$ , (b) 3M  $Zn(OTf)_2$ , (c) 3M  $ZnSO_4$ , (d) 2M  $Zn(SA)_2$ , and (e) 2M  $Zn(OAc)_2$ , (f) 1.6M  $Zn(PS)_2$ .

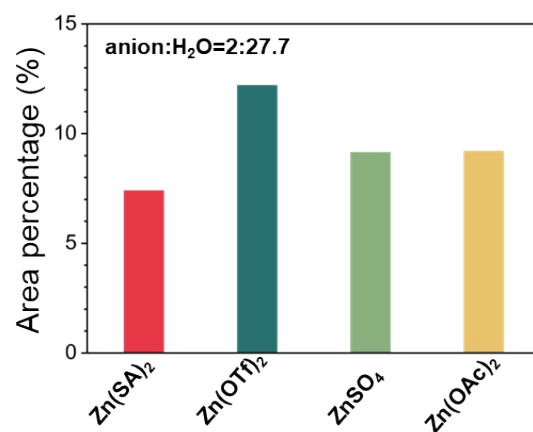


**Figure S2.** Relative proportions of isolated water in aqueous zinc electrolytes with fixed molar ratios of anion to water.

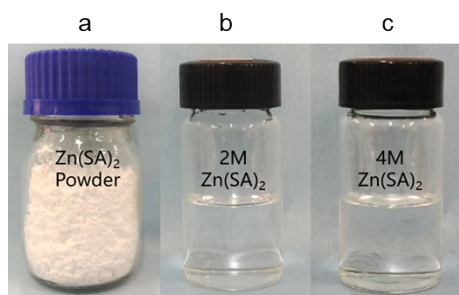


**Figure S3.** Synthesis of aqueous  $\text{Zn(SA)}_2$  electrolytes: (a)  $\text{Zn(SA)}_2$  salt, (b) 2M  $\text{Zn(SA)}_2$ , (c) 4M  $\text{Zn(SA)}_2$  (saturated).

**Table S1.** Summary of the vibrational peaks for SA powder,  $\text{Zn(SA)}_2$  powder, and  $\text{Zn(SA)}_2$  solutions<sup>13,14</sup>.

Peak Assignment	SA powder	$\text{Zn(SA)}_2$ powder	2M $\text{Zn(SA)}_2$	4M $\text{Zn(SA)}_2$	100 cycles	1 <sup>st</sup> -discharge	1 <sup>st</sup> -charge
-OH stretching					3567	3568	3568
-OH stretching		3495			3482	3483	3479
-OH stretching					3454	3450	
-OH stretching					3408	3413	3403
OH stretching		3352	3362	3343			
-NH <sub>2</sub> stretching		3268					
-NH <sub>2</sub> stretching							
-NH <sub>2</sub> stretching		3180			3180	3179	3163
NH <sub>3</sub> <sup>+</sup> and -NH <sub>2</sub>	3125						
NH <sub>3</sub> <sup>+</sup> and -NH <sub>2</sub>		3053			3087	3088	3075
Symmetric NH <sub>3</sub> <sup>+</sup> stretching	2877				2845	2850	2846
N-H stretching	2573						
-OH bending		1640	1642	1645	1638		
Degen. NH <sub>3</sub> <sup>+</sup> deformation	1541	1540	1559	1557	1535	1548	1550
Symmetric NH <sub>3</sub> <sup>+</sup> deformation	1438				1429	1420	1422
S=O	1304	1313			1311	1313	1317
Asymmetric -SO <sub>3</sub> <sup>-</sup> stretching	1257	1266	1245	1245	1240	1248	1258
Symmetric -SO <sub>3</sub> <sup>-</sup> stretching	1067	1052	1048	1048	1037	1039	1047
Degen. NH <sub>3</sub> <sup>+</sup> rocking	1003				1001	1001	
N-S stretching	689				704	710	
Degen. -SO <sub>3</sub> <sup>-</sup> deformation	542	562	562	562	562	560	

For the synthesized  $\text{Zn(SA)}_2$  powder, the peaks of  $3272\text{cm}^{-1}$  can be attributed to the stretching vibration of  $\text{NH}_2$ , with reference to the symmetric vibration of  $\text{NH}_3^+$  at  $3125\text{cm}^{-1}$  and  $2877\text{cm}^{-1}$  for SA. The peak at  $1540\text{cm}^{-1}$  is attributed to the degenerate  $\text{NH}_3^+$  deformation, originating from the degenerate  $\text{NH}_3^+$  deformation at  $1541\text{cm}^{-1}$  and the symmetric  $\text{NH}_3^+$  deformation at  $1438\text{cm}^{-1}$  in SA powder. Also, a blue shift of asymmetric  $-\text{SO}_3^-$  stretching was found in  $\text{Zn(SA)}_2$  powder of  $1321$  and  $1266\text{cm}^{-1}$  compared with  $1304$  and  $1257\text{cm}^{-1}$  for SA, with a red shift of symmetric  $-\text{SO}_3^-$  deformation at  $1052\text{cm}^{-1}$  compared with  $1067\text{cm}^{-1}$  for SA.

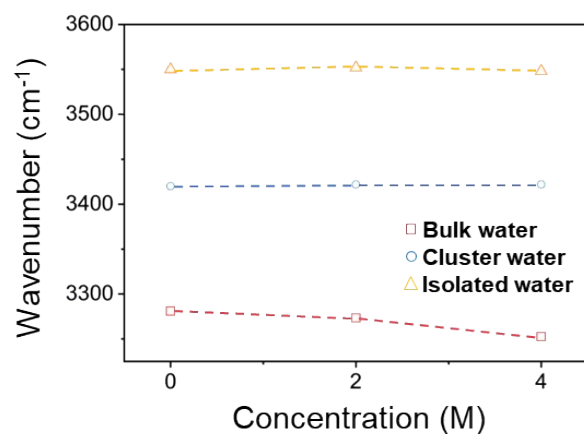


**Figure S4.** Deconvoluted peak positions of different water states, considering DI H<sub>2</sub>O, 2M Zn(SA)<sub>2</sub>, and 4M Zn(SA)<sub>2</sub>. Peak position of bulk water red-shifts from 3266 cm<sup>-1</sup> to 3252 cm<sup>-1</sup>, when the concentration increases from 2M to 4M.

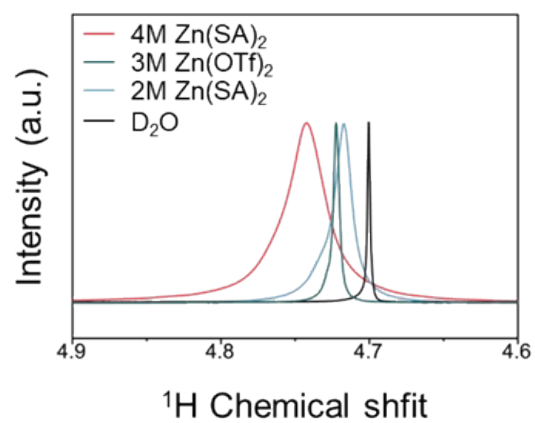


**Figure S5.**  $^1\text{H}$  NMR spectra of  $\text{D}_2\text{O}$  and aqueous zinc electrolytes.

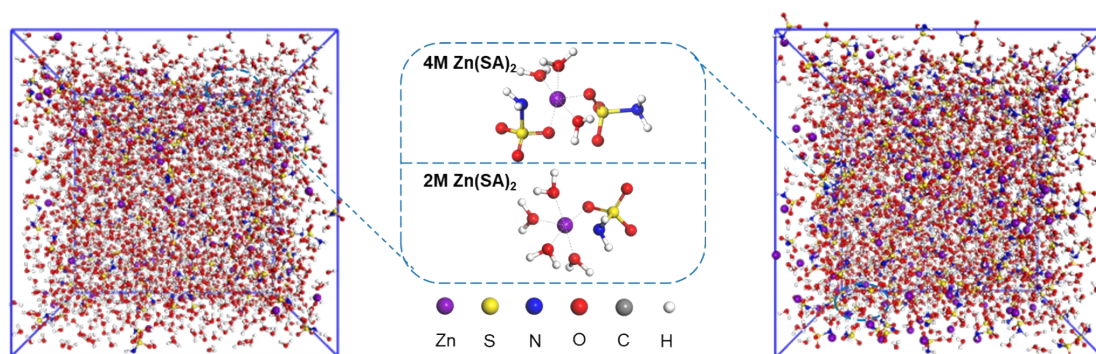


**Figure S6.** MD snapshots displays the solvation structure of 4M Zn(SA)<sub>2</sub>, where Zn<sup>2+</sup> is coordinated with three H<sub>2</sub>O molecules and two SA<sup>-</sup> in 4M Zn(SA)<sub>2</sub>.

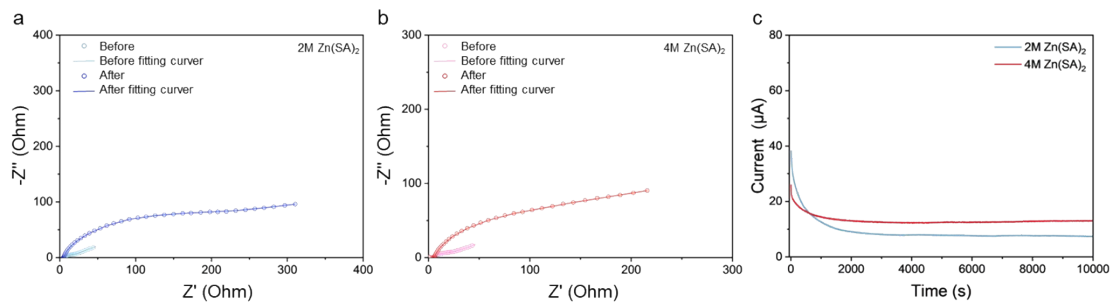


**Figure S7.** Nyquist plots before and after the polarizations test for (a) 4M Zn(SA)<sub>2</sub> and (b) 2M Zn(SA)<sub>2</sub>. (c) Current-time curves of the Zn|Zn symmetric cells at room temperature with constant polarization ( $\Delta V = 10$  mV) using Zn(SA)<sub>2</sub> electrolytes.

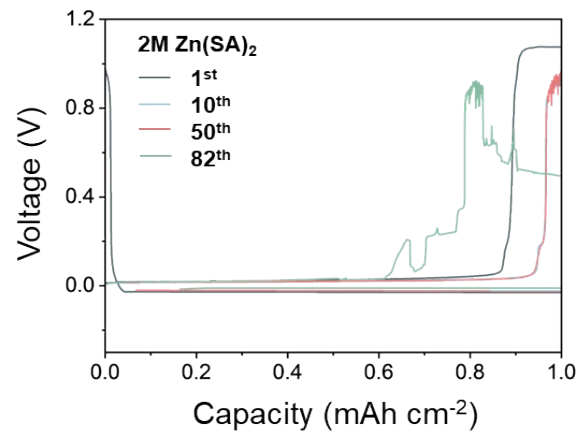


**Figure S8.** Voltage profile of the Cu|Zn cell in 2M Zn(SA)<sub>2</sub> at 1 mA cm<sup>-2</sup> and 1 mAh cm<sup>-2</sup>.

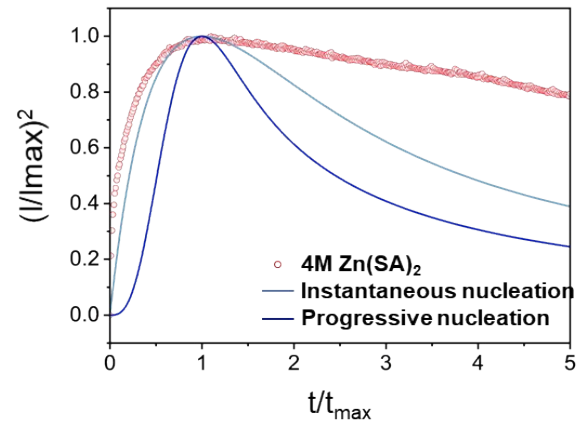


**Figure S9.** Scharifker–Hills model allows determining the type of nucleation by analyzing the ascending parts of the chronoamperometry, prior to the overlap of nuclei diffusion zones. By Scharifker–Hills analysis, CA of 4M Zn(SA)<sub>2</sub> approaches the predicted curve by the instantaneous nucleation theory<sup>11</sup>.

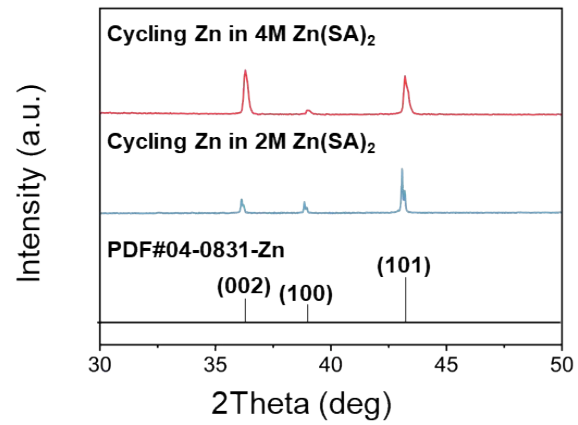


**Figure S10.** XRD patterns comparing the intensity ratios of  $I(002)/I(101)$  for Zn deposited at  $1 \text{ mA cm}^{-2}$  and  $1 \text{ mAh cm}^{-2}$  in 4M and 2M  $\text{Zn}(\text{SA})_2$ , which are 1.27 and 0.20, respectively.

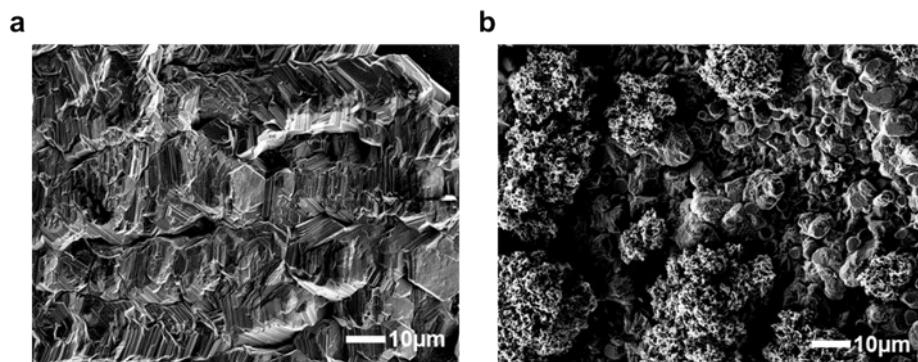


**Figure S11.** SEM images of the deposited Zn on Cu at  $10 \text{ mA cm}^{-2}$  and  $10 \text{ mAh cm}^{-2}$  for (a) 4M and (b) 2M  $\text{Zn(SA)}_2$ , respectively.

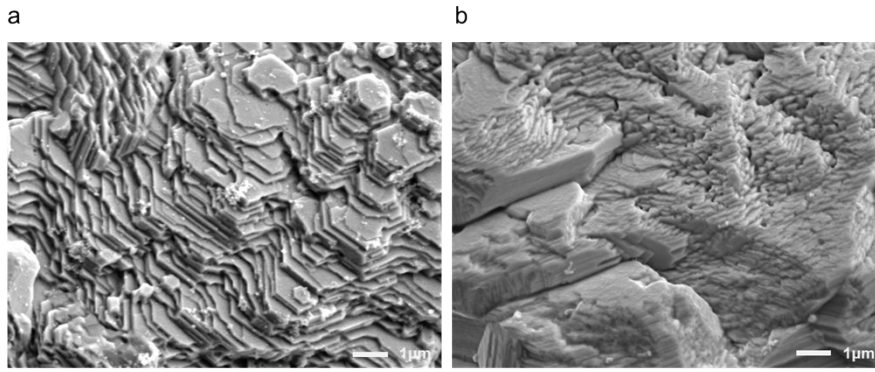


**Figure S12.** SEM images of the deposited Zn on Cu at  $1 \text{ mA cm}^{-2}$  and  $1 \text{ mAh cm}^{-2}$  for (a) 4M and (b) 2M  $\text{Zn(SA)}_2$ . Using a 4M  $\text{Zn(SA)}_2$  electrolyte, the Zn deposition on the Cu surface is uniform, exposing a large number of  $\text{Zn(002)}$  crystal planes, and the surface is flat. This is beneficial for suppressing the growth of Zn dendrites. In contrast, when using a 2M  $\text{Zn(SA)}_2$  electrolyte, the Zn deposition on Cu is non-uniform and irregular.

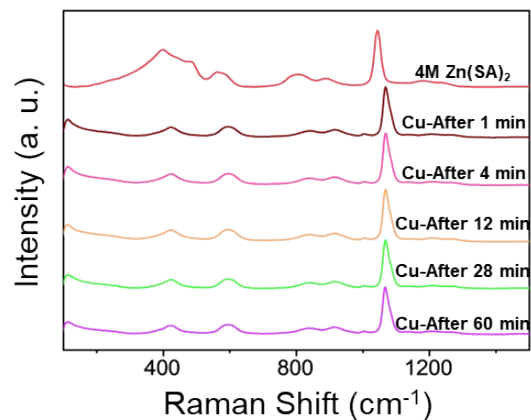


**Figure S13.** *in situ* Raman spectroscopy indicating the evolution of interfacial vibrational features during Zn deposition, with reference to those of bulk electrolyte 4M Zn(SA)<sub>2</sub>. The vibrational frequencies of O–S–O, Degen. –SO<sub>3</sub><sup>-</sup> deformation, symmetric –SO<sub>3</sub><sup>-</sup> stretching blue shift from 399, 576, 1043 cm<sup>-1</sup> for 4M Zn(SA)<sub>2</sub> to 426, 595, 1065 cm<sup>-1</sup> for those at the interface, respectively.

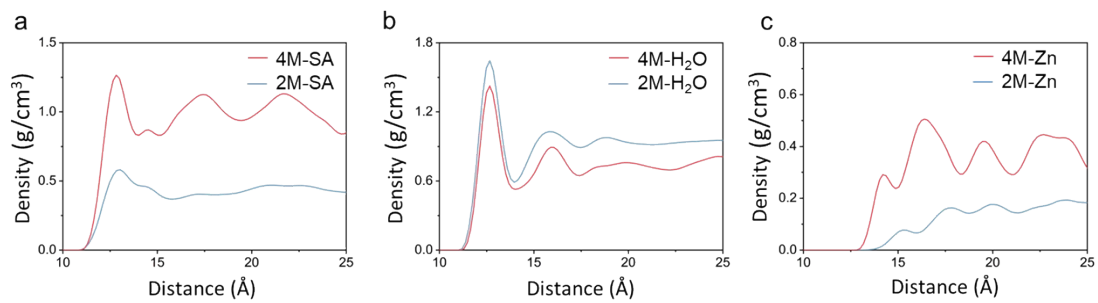


**Figure S14.** Density distributions of (a) SA<sup>-</sup>anion, (b) H<sub>2</sub>O, and (c) Zn<sup>2+</sup> ions at the interface, comparing 2M and 4M Zn(SA)<sub>2</sub>.

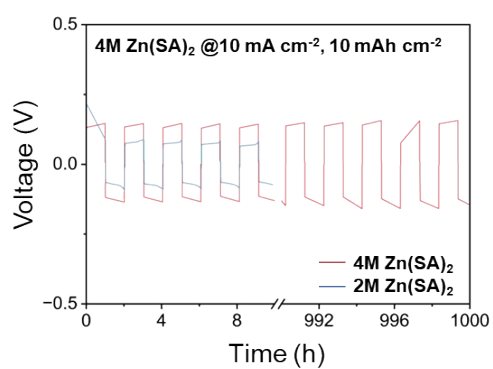


**Figure S15.** The polarization voltage comparing the cells with Zn(SA)<sub>2</sub> electrolytes at 10 mA cm<sup>-2</sup> and 10 mAh cm<sup>-2</sup>. The polarization with 4M Zn(SA)<sub>2</sub> is ~262 mV for the first 10 cycles, and stabilizes at ~202 mV.

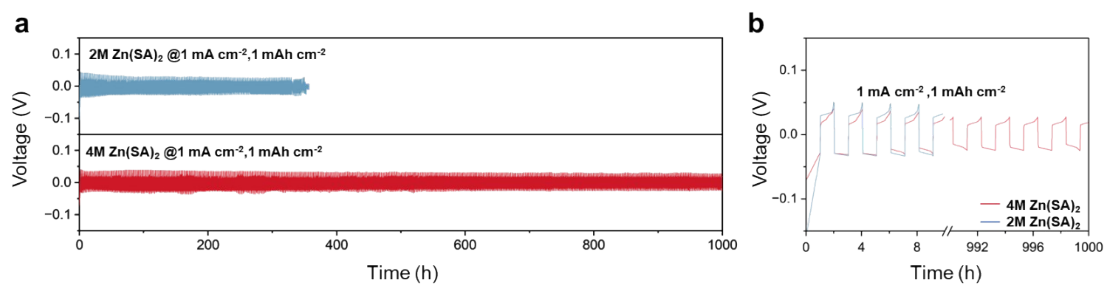


**Figure S16.** (a) Zn stripping/plating of the Zn|Zn cell at 1 mA cm<sup>-2</sup> and 1 mAh cm<sup>-2</sup>. The symmetric cell with 2M Zn(SA)<sub>2</sub> shorts at ~352 h. In contrast, the cell with 4M Zn(SA)<sub>2</sub> can last for ~1000 h, with stable overpotentials through the cycling. (b) The polarization voltage for the first 10 cycles of the cell with 4M Zn(SA)<sub>2</sub> is ~59 mV, and for the cell with 2M Zn(SA)<sub>2</sub> is ~70 mV. Additionally, the polarization voltage for the last 10 cycles of the cell with 4M Zn(SA)<sub>2</sub> is ~41 mV.

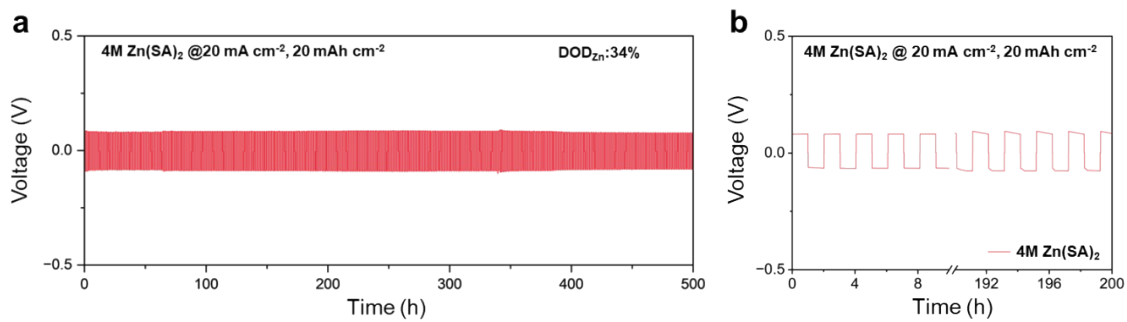


**Figure S17.** (a) Galvanostatic Zn stripping/plating in the Zn|Zn cell at 20 mA cm<sup>-2</sup> and 20 mAh cm<sup>-2</sup>, with a DOD of ~34%. (b) The polarization voltage comparing the cells with 4M Zn(SA)<sub>2</sub> at 20 mA cm<sup>-2</sup> and 20 mAh cm<sup>-2</sup>. The polarization with 4M Zn(SA)<sub>2</sub> for the first 10 cycles is ~175 mV, which stabilizes ~157 mV.

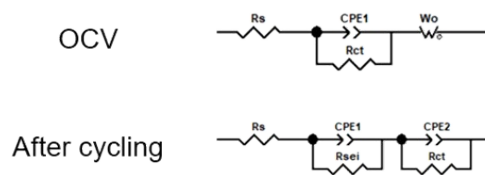


**Figure S18.** Equivalent circuits for EIS spectra of Zn|Zn at OCV and after cycling.

Ionic conductivity ( $\sigma$ ) of the SEI was estimated according to the equation of  $\sigma=L/RS$ , where R represents the impedance of the SEI measured according to EIS, L represents the thickness of the SEI ( $1.8 \times 10^{-3}$  cm), and S is the surface area ( $2.01$  cm<sup>2</sup>).

For SEI by 4M Zn(SA)<sub>2</sub>,  $\sigma_{SEI} = 0.26$  mS cm<sup>-1</sup>.

**Table S2.** Summary of the EIS data fitting for the symmetric cells with 4M and 2M Zn(SA)<sub>2</sub> electrolytes.

Electrolyte	Test condition	R <sub>0</sub>	R <sub>SEI</sub>	R <sub>CT</sub>
2M Zn(SA) <sub>2</sub>	OCV	1.58		17.73
4M Zn(SA) <sub>2</sub>	OCV	0.86		7.63
2M Zn(SA) <sub>2</sub>	After cycling	6.89	14.41	56.4
4M Zn(SA) <sub>2</sub>	After cycling	3.44	13.92	37.74

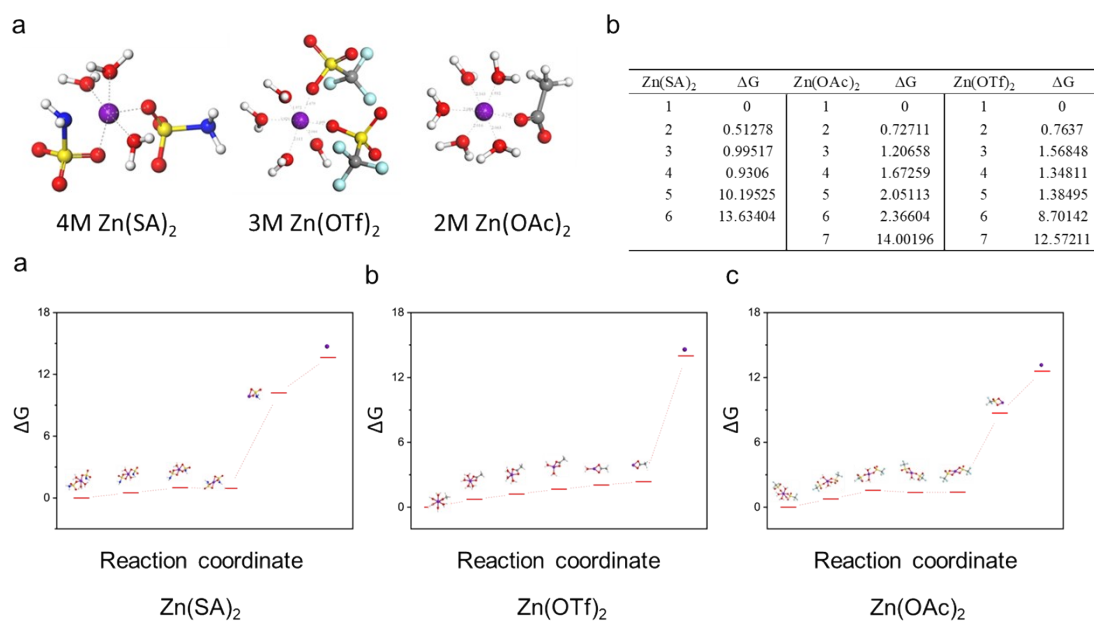


**Figure S19** (a) Solvation structure of the saturated Zn(SA)<sub>2</sub>, Zn(OTf)<sub>2</sub>, Zn(OAc)<sub>2</sub> aqueous electrolytes. (b) The list of desolvation energy barriers for the saturated zinc electrolytes, with (c, d, e) their individual specific desolvation steps.

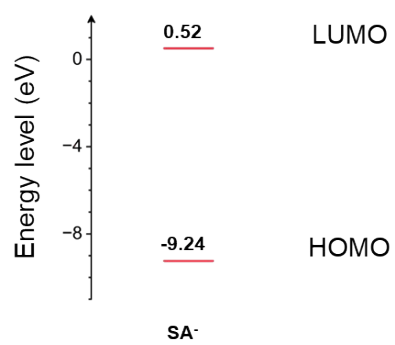


**Figure S20.** Calculated LUMO and HOMO of SA<sup>-</sup>.

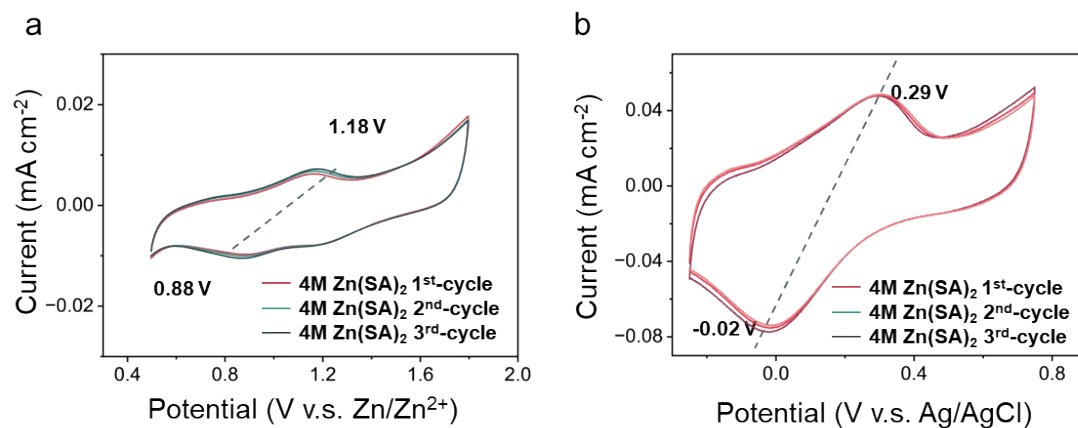


**Figure S21.** CV spectra considering 4M Zn(SA)<sub>2</sub> at a scan rate of 0.1 mV s<sup>-1</sup> conducted by (a) Pt/Zn 2-electrode and (b) Graphite/Pt 3-electrode. Reduction and oxidation peaks were observed at 0.88 V v.s. Zn/Zn<sup>2+</sup> (-0.02 V v.s. Ag/AgCl) and 1.18 V v.s. Zn/Zn<sup>2+</sup> (0.29 V v.s. Ag/AgCl), respectively.

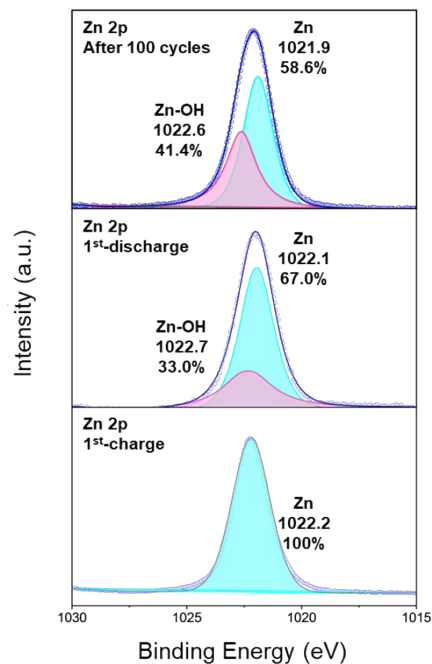


**Figure S22.** XPS spectra of Zn2*p* for the cycled surface after 1<sup>st</sup>-charge, 1<sup>st</sup>-discharge, and 100<sup>th</sup> cycles.

The Zn<sup>0</sup> peaks after 1<sup>st</sup>-discharge and 100<sup>th</sup> cycles exhibit a red shift of 0.1 eV and 0.3 eV, respectively, relative to the one after 1<sup>st</sup>-charge peak at 1022.2 eV. This red shift can be attributed to the oxidation of the metal surface. After cycling, a higher peak at ~1022.6 eV is detected, which can be attributed to Zn-OH. As cycling proceeds, the proportion of Zn-OH increases from 33.0% in the 1<sup>st</sup> discharge to 41.4% after 100 cycles.

**Table S3.** Summary of the fitted peaks of S2p and N1s in XPS spectra for 1<sup>st</sup>-discharge, 1<sup>st</sup>-charge and after 100<sup>th</sup> cycles in 4M Zn(SA)<sub>2</sub>, respectively.

Sample	Component	Binding Energy(eV)	Area percentage (%)
S 2p-1 <sup>st</sup> -discharge	NH <sub>2</sub> SO <sub>3</sub> <sup>-</sup>	170.3	31.2
S 2p-1 <sup>st</sup> -discharge	NH <sub>2</sub> SO <sub>3</sub> <sup>-</sup>	169.2	59.6
S 2p-1 <sup>st</sup> -discharge	SO <sub>3</sub> <sup>-</sup>	167.8	9.2
S 2p-1 <sup>st</sup> -charge	NH <sub>2</sub> SO <sub>3</sub> <sup>-</sup>	170	29
S 2p-1 <sup>st</sup> -charge	NH <sub>2</sub> SO <sub>3</sub> <sup>-</sup>	168.7	71
S 2p-after 100 <sup>th</sup> cycle	NH <sub>2</sub> SO <sub>3</sub> <sup>-</sup>	170.2	20
S 2p-after 100 <sup>th</sup> cycle	NH <sub>2</sub> SO <sub>3</sub> <sup>-</sup>	168.8	67.8
S 2p-after 100 <sup>th</sup> cycle	SO <sub>3</sub> <sup>-</sup>	166.7	12.2
N 1s-1 <sup>st</sup> -discharge	-NH <sub>2</sub>	400.8	24.2
N 1s-1 <sup>st</sup> -discharge	N-S	399.9	59.8
N 1s-1 <sup>st</sup> -discharge	N-S	398.4	15.9
N 1s-1 <sup>st</sup> -charge	N-S	399.2	93.9
N 1s-1 <sup>st</sup> -charge	N-S	397.3	6.1
N 1s-after 100 <sup>th</sup> cycle	-NH <sub>2</sub>	399.5	37.9
N 1s-after 100 <sup>th</sup> cycle	N-S	398.9	23.8
N 1s-after 100 <sup>th</sup> cycle	N-S	397.7	38.3

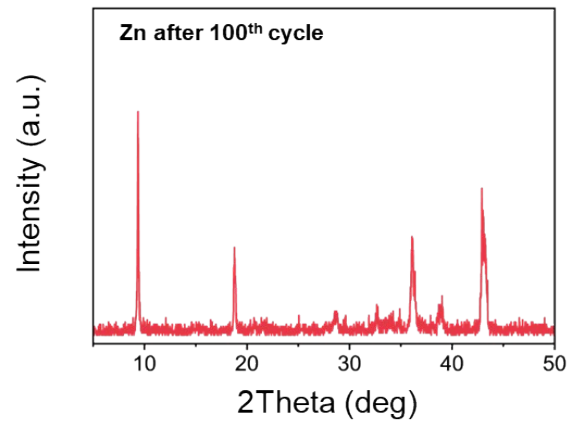


**Figure S23.** XRD pattern of the cycled Zn after 100 cycles in Zn|Zn with 4M Zn(SA)<sub>2</sub>.

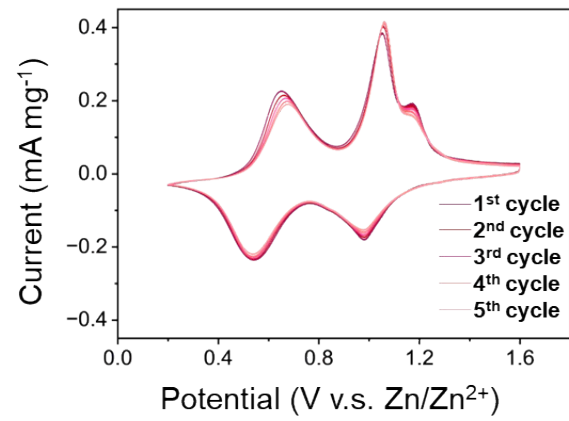


**Figure S24.** CV curves of the  $V_2O_5/Zn$  cell with 4M  $Zn(SA)_2$  electrolyte at a scan rate of  $0.1 \text{ mV s}^{-1}$  in the first five cycles.

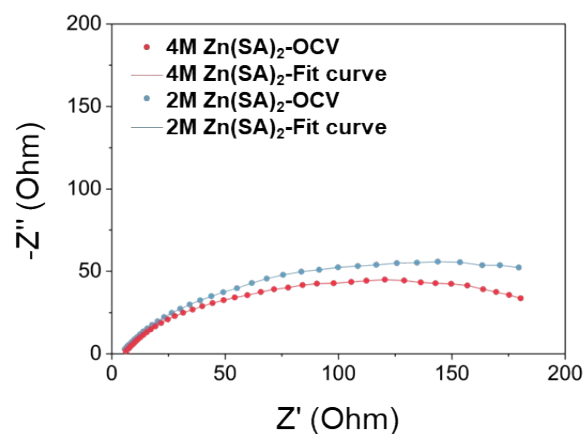


**Figure S25.** EIS spectra of the full cells with 2M and 4M Zn(SA)<sub>2</sub>.

**Table S4.** Equivalent circuits for OCV, with the fitted data for 2M and 4M Zn(SA)<sub>2</sub>.



Electrolyte	Test condition	R <sub>0</sub>	R <sub>SEI</sub>	R <sub>CT</sub>
2M Zn(SA) <sub>2</sub>	OCV	4.1	46.4	200.2
4M Zn(SA) <sub>2</sub>	OCV	5.3	44.8	165.4

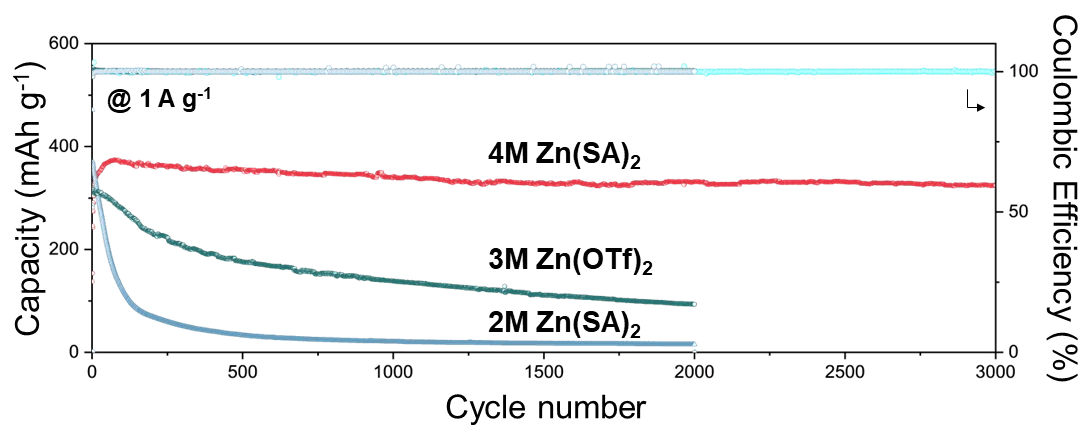


**Figure S26.** Cycling performance of the cells comparing zinc electrolytes at 1 A g<sup>-1</sup>.

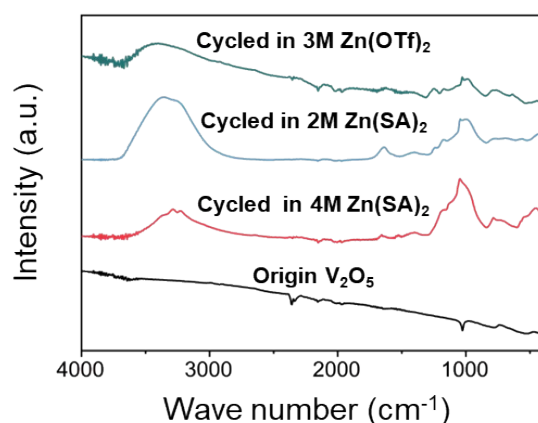


**Figure S27.** Corresponding FTIR spectra of the cathodes after cycling. In the original  $V_2O_5$ , the vibrational peaks at  $\sim 453$ ,  $705$ , and  $979\text{ cm}^{-1}$  are assigned to the stretching modes of VOBV, VOC, and the in-plane stretching mode of the terminal VOA, respectively. The peaks at  $705$  and  $550\text{ cm}^{-1}$  reflect the reduced state of  $V^{5+}$ , consistent with the synthesized mixed-valence  $V_2O_5$ . Additionally, it indicates the presence of  $-\text{SO}_3^-$  and  $\text{NH}_3^+$  groups on the cathode surface.

**Table S5.** Summary of the vibrational peaks of the pristine  $V_2O_5$ ,  $V_2O_5$  after cycling in  $4\text{M Zn}(\text{SA})_2$ ,  $2\text{M Zn}(\text{SA})_2$ , and  $3\text{M Zn}(\text{OTf})_2$ , respectively.

Peak Assignment	$V_2O_5$ -3M $Zn(\text{OTf})_2$	$V_2O_5$ -2M $Zn(\text{SA})_2$	$V_2O_5$ -4M $Zn(\text{SA})_2$	$V_2O_5$
Symmetric $\text{SO}_3^-$ deformation	1028	1043	1045	
Degen. $\text{NH}_3^+$ rocking				
stretching, $V(\equiv)\text{O}(\text{A})$	985	985	987	979
stretching, $V(\equiv)\text{O}(\text{A})$				952
$\text{NH}_2$ group				
V-O-V, bending vibration	880	880		
O-S-O, bending vibration	792	785	785	
V- $\text{H}_2\text{O}$	742	711	715	738
O-S-O, bending vibration			719	
stretching, V-O(C)	705	704	705	705
stretching, V-O(C)				675
stretching, V-O(C)				661
N-S stretching				
O-S-O, bending vibration				
Zn-O, stretching vibration				
stretching, V-O(C)	592	582	574	578
stretching, V-O(C)	561	557	550	550
Degen. $\text{SO}_3^-$ deformation				
bending, $\delta(\text{V-O3-V})$ (B)	443	455	453	457
O-S-O, bending vibration	410	410	410	

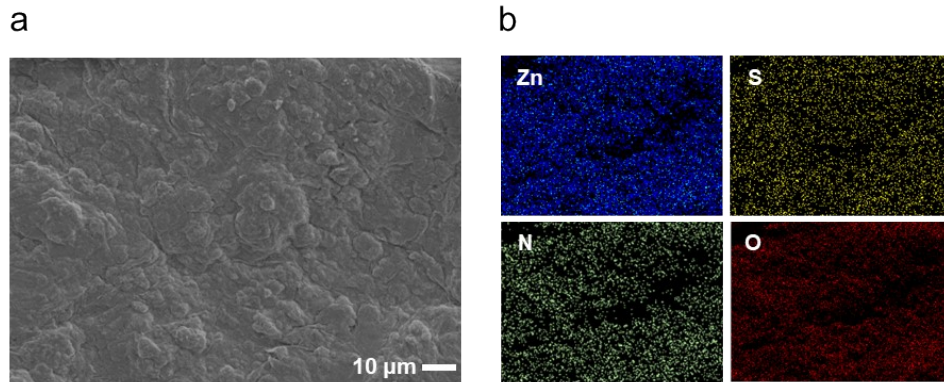


**Figure S28.** (a) SEM image reveals that the cycled  $V_2O_5$  is uniformly covered by the surface layer, (b) consisting of Zn, S, N, and O.

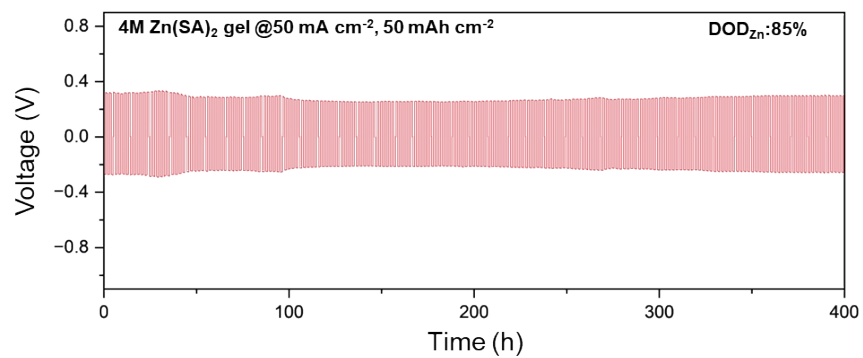


**Figure S29.** Zn|Zn cell with 4M Zn(SA)<sub>2</sub>@PAAm gel at 50 mA cm<sup>-2</sup> and 50 mAh cm<sup>-2</sup>, with a DOD of ~ 85%.

**Table S6.** Cost estimation on the Zn(SA)<sub>2</sub>-based gel and eutectic electrolyte.

Materials	Species	Purity (%)	Price (\$ g <sup>-1</sup> )	Cost (1mol Zn <sup>2+</sup> /)\$
Gel electrolytes				
Sulfamic acid	Acid	99	0.16	31.07
Zinc oxide	Basic oxides	99	0.016	1.3
Polyacrylamide	Polymer	99	0.017	1.13
Potassium persulfate	Initiators	99	0.041	0.009
N,N'-Methylenebis(acrylamide)	Adhesives	99	0.076	0.017
$\alpha$ -Ketoglutaric acid	Additive	98	0.12	0.089
Deep eutectic electrolytes				
Sulfamic acid	Acid	99	0.16	31.07
Zinc oxide	Basic oxides	99	0.016	1.3
Ethylene glycol	Organic solvent	98	0.014	13.77
Glycerol	Organic solvent	98	0.014	13.77

## References

- 1 Sun, H., Ren, P. & Fried, J. R. The COMPASS force field: parameterization and validation for phosphazenes. *Computational and Theoretical Polymer Science* **8**, 229-246 (1998).
- 2 Sun, H. COMPASS: An ab Initio Force-Field Optimized for Condensed-Phase Applications Overview with Details on Alkane and Benzene Compounds. *The Journal of Physical Chemistry B* **102**, 7338-7364 (1998).
- 3 Borodin, O. *et al.* Competitive lithium solvation of linear and cyclic carbonates from quantum chemistry. *Physical Chemistry Chemical Physics* **18**, 164-175 (2016).
- 4 Qu, Z. *et al.* Designing C-Fe-O bonded MIL-88B(Fe)/jasmine petal-derived-carbon composite biosensor for the simultaneous detection of dopamine and uric acid. *Chemical Engineering Journal* **404**, 126570 (2021).
- 5 Zhang, X.-Q. *et al.* Highly Stable Lithium Metal Batteries Enabled by Regulating the Solvation of Lithium Ions in Nonaqueous Electrolytes. *Angewandte Chemie International Edition* **57**, 5301-5305 (2018).
- 6 Moore, G. W. K., Howell, S. E. L., Brady, M., Xu, X. & McNeil, K. Anomalous collapses of Nares Strait ice arches leads to enhanced export of Arctic sea ice. *Nature Communications* **12**, 1 (2021).
- 7 Yan, C. *et al.* Regulating the Inner Helmholtz Plane for Stable Solid Electrolyte Interphase on Lithium Metal Anodes. *Journal of the American Chemical Society* **141**, 9422-9429 (2019).
- 8 Huang, C. *et al.* Stabilizing Zinc Anodes by Regulating the Electrical Double Layer with Saccharin Anions. *Advanced Materials* **33**, 2100445 (2021).
- 9 Evans, J., Vincent, C. A. & Bruce, P. G. Electrochemical measurement of transference numbers in polymer electrolytes. *Polymer* **28**, 2324-2328 (1987).
- 10 Wu, F. *et al.* "Liquid-in-Solid" and "Solid-in-Liquid" Electrolytes with High Rate Capacity and Long Cycling Life for Lithium-Ion Batteries. *Chemistry of Materials* **28**, 848-856 (2016).
- 11 Benea, L. & Danaila, E. Nucleation and Growth Mechanism of Ni/TiO<sub>2</sub> Nanoparticles Electro-Codeposition. *Journal of The Electrochemical Society* **163**, D655, doi:10.1149/2.0591613jes (2016).
- 12 Zhao, J. *et al.* High-performance flexible quasi-solid-state zinc-ion batteries with layer-expanded vanadium oxide cathode and zinc/stainless steel mesh composite anode. *Nano Energy* **62**, 94-102 (2019).
- 13 Kazachenko, A. S. *et al.* Sulfamic acid/water complexes (SAA-H<sub>2</sub>O(1-8)) intermolecular hydrogen bond interactions: FTIR, X-ray, DFT and AIM analysis. *Journal of Molecular Structure* **1265**, 133394 (2022).
- 14 Kumar, R. *et al.* Sulphamic acid: potential single crystal for nonlinear optical applications. *Journal of Materials Science: Materials in Electronics* **31**, 14271-14278 (2020).